

Finding dusty AGNs from the *JWST* CEERS survey with mid-infrared photometry

Tom C.-C. Chien^{1,*}, Chih-Teng Ling², Tomotsugu Goto^{1,2}, Cossas K.-W. Wu², Seong Jin Kim², Tetsuya Hashimoto³, Yu-Wei Lin¹, Ece Kilerci⁴, Simon C.-C. Ho^{5,6,7,8}, Po-Ya Wang¹, and Bjorn Jasper R. Raquel^{3,9}

¹Department of Physics, National Tsing Hua University, 101, Section 2, Kuang-Fu Road, Hsinchu, 30013, Taiwan (R.O.C.)

²Institute of Astronomy, National Tsing Hua University, 101, Section 2, Kuang-Fu Road, Hsinchu, 30013, Taiwan (R.O.C.)

³Department of Physics, National Chung Hsing University, 145, Xingda Road, Taichung, 40227, Taiwan (R.O.C.)

⁴Sabancı University, Faculty of Engineering and Natural Sciences, 34956, Istanbul, Turkey

⁵Research School of Astronomy and Astrophysics, The Australian National University, Canberra, ACT 2611, Australia

⁶Centre for Astrophysics and Supercomputing, Swinburne University of Technology, P.O. Box 218, Hawthorn, VIC 3122, Australia

⁷OzGrav: The Australian Research Council Centre of Excellence for Gravitational Wave Discovery, Hawthorn, VIC 3122, Australia

⁸ASTRO3D: ARC Centre of Excellence for All-sky Astrophysics in 3D, ACT 2611, Australia

⁹National Institute of Physics, College of Science, University of the Philippines, Diliman, Quezon City, 1101 Metro Manila, Philippines

Accepted 2024 June 19. Received 2024 June 17; in original form 2023 September 29

ABSTRACT

The nature of the interaction between active galactic nuclei (AGNs) and their host galaxies remains an unsolved question. Therefore, conducting an AGN census is valuable to AGN research. Nevertheless, a significant fraction of AGNs are obscured by their environment, which blocks UV and optical emissions due to the dusty torus surrounding the central supermassive black hole (SMBH). To overcome this challenge, mid-infrared (IR) surveys have emerged as a valuable tool for identifying obscured AGNs, as the obscured light is re-emitted in this range. With its high sensitivity, the James Webb Space Telescope (*JWST*) uncovered more fainter objects than previous telescopes. By applying the SED fitting, this work investigates AGN candidates in *JWST* Cosmic Evolution Early Release Science (CEERS) fields. We identified 42 candidates, 30 of them are classified as composites ($0.2 \leq f_{\text{AGN,IR}} < 0.5$), and 12 of them are AGNs ($f_{\text{AGN,IR}} \geq 0.5$). We report the AGN luminosity contributions and AGN number fractions as a function of redshift and total infrared luminosity, showing that previously reported increasing relations are not apparent in our sample due to the sample size. We also extend the previous results on ultra-luminous infrared galaxies (ULIRGs, $L_{\text{TIR}} \geq 10^{12} L_{\odot}$) to less luminous AGNs, highlighting the power of *JWST*.

Key words: galaxies: active, high redshift, nuclei - infrared: galaxies

1 INTRODUCTION

Active galactic nuclei (AGNs) are one of the most intriguing and challenging phenomena in modern astronomy. Supermassive black holes (SMBHs) residing in AGNs trigger many spectacular phenomena (e.g., relativistic jets, Blandford et al. 2019), brightening AGNs and influencing the evolution of their host galaxies. Therefore, studying AGNs provides a valuable way to understand the co-evolution of SMBHs and their host galaxies, which is crucial for understanding how galaxies evolve. There are several features in AGNs according to the AGN unification model (e.g., Netzer 2015), for instance, accretion disc around centre SMBH, broad line and narrow line region, and dusty torus which is more outer than accretion disc. One of the important features is the hot accretion disk around SMBH, which emits UV/optical radiation. Nevertheless, due to the obscuration by the surrounding dust, the majority of AGNs are missed in UV and optical bands, and even hard X-ray emission could be obscured

in a Compton-thick AGN (e.g., Comastri 2004). Due to the nature of obscuration in these bands, it is usually difficult to find dusty AGNs directly. To prevent missing obscured objects, a mid-infrared (mid-IR) observation survey becomes significant when researching obscured AGNs (e.g., Chang et al. 2017; Wang et al. 2020). Additionally, several studies have reported a strong correlation between mid-infrared (mid-IR) luminosity and X-ray luminosity (e.g., Auge et al. 2023), showing the significance and effectiveness of mid-IR observations in probing AGNs.

The absorbed UV/optical light can be re-emitted in mid-IR wavelengths by the surrounding dusty environments. Such environments make the obscured AGNs extinction-less in mid-IR wavelengths. Besides, the majority of the high redshift (high- z) galaxies are identified as obscured objects (e.g., Treister et al. 2010). Their existence is substantial for probing the history of SMBHs, which further connects to the black hole accretion history (BHAH, e.g., Yang et al. 2023b). Therefore, understanding the properties of AGNs allows the study to investigate the history of centre SMBHs and explore the co-evolution between SMBHs and their host galaxies. Nevertheless, it is worth not-

* E-mail: minoodos90214@gmail.com

ing that the emission of polycyclic aromatic hydrocarbon (PAH) in mid-IR wavelengths produced by star-forming galaxies (SFGs) is an issue in identifying AGNs (Feltre et al. 2013; Kim et al. 2019). It substantially impacts the identification by mimicking AGN emissions in mid-IR wavelength. To avoid such sample contamination, spectral energy distribution (SED) is a powerful tool that allows us to significantly divide SFGs and AGNs. For instance, Yang et al. (2023b) applied Code Investigating GALaxy Emission v2022.1 (CIGALE; Boquien et al. 2019), a SED fitting code, to analysed and classified observed sources into AGNs, composites, and SFGs. They also utilised the physical properties estimated from CIGALE to depict the BHAH.

With mid-IR observation, it is possible to unearth obscured AGNs due to the strong emission from their dusty torus. Recently, the state-of-the-art IR telescope, James Webb Space Telescope (*JWST*) provided an unprecedented sensitivity to observe fainter galaxies. The Mid-Infrared Instrument (MIRI, Rieke et al. 2015; Rigby et al. 2023) is the main instrument to study obscured AGNs. Lyu et al. (2024) utilised MIRI in Systematic Mid-infrared Instrument Legacy Extragalactic Survey (SMILES, Rieke et al. 2017) and identified a surprisingly large number of new obscured AGNs (~80% among their 217 candidates). This highlights the potential of *JWST* as the premier instrument for investigating obscured AGNs. Back to MIRI, it has a continuous coverage in the mid-IR region (from $5.6\mu\text{m}$ to $25.5\mu\text{m}$, 9 bands), which is much more sensitive than *AKARI* and the *Spitzer* up to 100 times they are (Wu et al. 2023; Ling et al. 2022).

Previous works reported an increasing AGN contribution trend with redshift (e.g., Wang et al. 2020; Chiang et al. 2019). Wang et al. (2020) performed an extinction-less census of AGNs in the North Ecliptic Pole (NEP, Matsuhara et al. 2006) with the *AKARI* space telescope (Murakami et al. 2007). The AGN contribution ($f_{\text{AGN,IR}}$, defined in equation 1) and AGN number fraction (f_{num} , defined in equation 2) are investigated in Wang et al. (2020) by utilising CIGALE for SED fitting, where an increasing trend with redshift for both quantities is reported. However, it is unclear if the trend is universal for AGNs in different total IR luminosity ranges. Chiang et al. (2019) provided an extinction-less census in the same survey as well, however, the SED fitting was performed by LEPHARE (Ilbert et al. 2006; Arnouts et al. 1999). The results were opposite to Wang et al. (2020). In this work, our goal is to examine the trend from Wang et al. (2020) still holds at higher redshift or lower luminosity with our AGN sample selected from the Cosmic Evolution Early Release Science (CEERS, Finkelstein et al. 2017; Yang et al. 2023a) survey. *JWST* provides more sensitive detection to observe fainter sources (Wu et al. 2023; Ling et al. 2022). We expect fainter sources that are invisible for previous space telescopes can extend Wang et al. (2020) and Chiang et al. (2019) researches to the faint end ($L_{\text{TIR}} \sim 10^{10}L_{\odot}$ or even fainter).

The structure of this paper is the following: We introduce the data processes, SED fittings, and sample selections in §2; In §3, we discuss the properties of our candidates based on our analysis results. The conclusion part summarises our main results, given in §4. We assume a cosmology based on Λ cold dark matter (Λ CDM) cosmology with $H_0 = 0.667$, $\Omega_m = 0.310$, $\Omega_b = 0.0490$, and $\Omega_{\Lambda} = 0.689$ (Planck Collaboration et al. 2020).

2 DATA AND ANALYSIS

2.1 MIR observations in CEERS and merged catalogue with CANDELS-EGS

JWST Cosmic Evolution Early Release Science (CEERS, Finkelstein et al. 2017; Yang et al. 2023a) survey provides a continuous observation from near-infrared (NIR) to mid-infrared (MIR) wavelength by *JWST* Near Infrared Camera (NIRcam), Mid-Infrared Instrument (MIRI, Rieke et al. 2015; Rigby et al. 2023), and Near-Infrared Spectrograph (NIRSpec).

In this work, we focus on 4 MIRI pointings in the Extended Groth Strip (EGS) legacy field with 6 continuous broad-band filters (F770W, F1000W, F1280W, F1500W, F1800W, and F2100W). Two pointings have all 6 bands (observation ID: o001_t021 and o002_t022), while the other two pointings have only 4 bands, missing F770W and F2100W (observation ID: o012_t026 and o015_t028). We use photometry reported in Wu et al. (2023) which conducts a series of processes including 80% completeness measurements and comparisons with previous model predictions (e.g., Gruppioni et al. 2011; Cowley et al. 2018). Besides, given that STScI has released the new MIRI flux calibration (see <https://www.stsci.edu/contents/news/jwst/2023/updates-to-the-miri-imager-flux-calibration-reference-files>), we have followed the manuscripts to update the photometry as well. The related updates are 15.0%, 4.1%, 0.8%, 1.2%, 3.3%, and 3.3% higher than previous for F770W, F1000W, F1280W, F1500W, F1800W, and F2100W, respectively. Wu et al. (2023)'s 80% completeness flux in CEERS survey are also scaled for F770W ($0.28\mu\text{Jy}$), F1000W ($0.65\mu\text{Jy}$), F1280W ($1.26\mu\text{Jy}$), F1500W ($2.0\mu\text{Jy}$), F1800W ($5.0\mu\text{Jy}$), and F2100W ($13.4\mu\text{Jy}$), respectively. More technical details are described in Wu et al. (2023).

To study the physical properties of AGNs, it is insufficient to utilise only MIR photometry. Therefore, a photometric catalogue covering multiple wavelengths is necessary. CANDELS-EGS Multi-wavelength catalogue (Stefanon et al. 2017) constructed from the Cosmic Assembly Near-IR Deep Extragalactic Legacy Survey (CANDELS: Grogin et al. 2011; Koekemoer et al. 2011) offers a broad observation range from near-UV to MIR in the EGS field. By matching our sources with CANDELS-EGS, we obtain a 21 multi-band catalogue with 15 bands from CANDELS-EGS and 6 bands from CEERS MIRI pointings (Ling et al. 2024, see Table 1 for details). Our catalogue includes 573 matched sources, each with at least one MIRI detection.

2.2 CIGALE SED fittings

Code Investigating GALaxy Emission v2022.1 (CIGALE; Boquien et al. 2019) is a Python-based code for fitting spectral energy distributions (SEDs) and can estimate the physical properties of galaxies with observations from far-UV to radio emission. It provides various modules such as star-forming history, dust attenuation, dust model, and AGN model to fit observations. In this work, we mainly follow the configuration from Yang et al. (2023b). We slightly change the number of AGN fractions, the dust attenuation model, and the given redshift. In Table B1, we list the details for the full parameters we adopt.

Note that in CIGALE, AGN contribution is called AGN fraction. Other literature might treat AGN fraction as AGN number fraction (e.g., Gu et al. 2018), which is another main discussion in this work. To avoid confusion, here, we use the term AGN contribution to replace the AGN fraction.

Telescope	Instrument	Bands	Reference
CFHT	MegaCam	u^*, g', r', i', z'	Gwyn (2012)
CFHT	WIRCam	J, H, Ks	Bielby et al. (2012)
<i>HST</i>	ACS	F606W, F814W	Koekemoer et al. (2011)
<i>HST</i>	WFC3	F125W, F160W	Koekemoer et al. (2011)
<i>HST</i>	WFC3	F140W	Skelton et al. (2014)
<i>Spitzer</i>	IRAC	$3.6\mu\text{m}, 4.5\mu\text{m}$	Ashby et al. (2015)
<i>JWST</i>	MIRI	F770W, F1000W, F1280W, F1500W, F1800W, F2100W	Ling et al. (2024); Wu et al. (2023)

Table 1. The details of bands used in merged multi-wavelength catalogue.

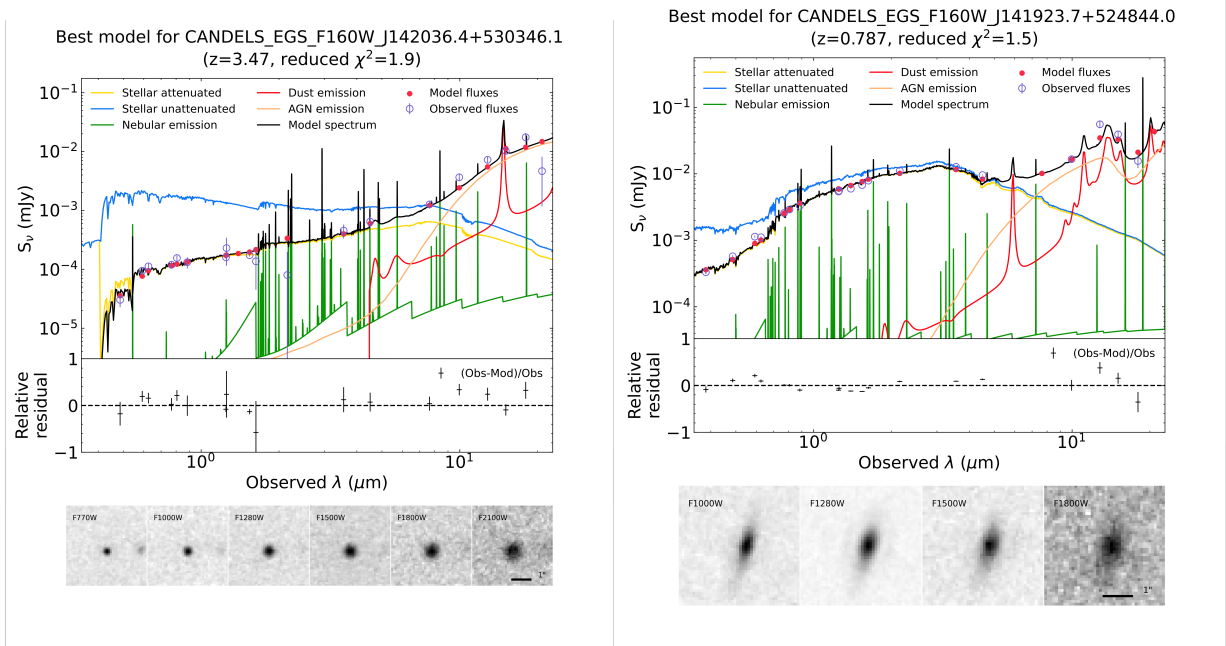


Figure 1. Two SEDs for AGN ($f_{\text{AGN,IR}} \geq 0.5$, left panel) and composite ($0.2 \leq f_{\text{AGN,IR}} < 0.5$, right panel) galaxy SED fitting examples from CIGALE and their cutout. The black line is the fitting curve; The red line is the dust emission, and the orange line is the AGN emission. The AGN contributions are $f_{\text{AGN,IR}} = 0.66 \pm 0.21$ and $f_{\text{AGN,IR}} = 0.30 \pm 0.20$, respectively.

AGN contribution ($f_{\text{AGN,IR}}$) is the ratio between AGN luminosity (L_{AGN}) and total infrared luminosity, describing how much the AGN emission contributes to the total emission. The definition of it is described in equation 1:

$$f_{\text{AGN,IR}} = \frac{L_{\text{AGN}}}{L_{\text{TIR}}} \quad (1)$$

where IR is defined in $8 - 1000\mu\text{m}$ by Kennicutt 1998. The default wavelength range to define the AGN contribution in CIGALE is $8\mu\text{m} - 1000\mu\text{m}$. Note that the total IR luminosity estimated by CIGALE might have uncertainty due to a lack of far-infrared (FIR) observations in this work. The relative problems will be discussed in §3.1. Additionally, since our sample selection criterion of the AGN contribution is $f_{\text{AGN,IR}} \geq 0.2$ (described in §2.3), we add extra choices of AGN contributions of 0.13, 0.15, and 0.18 during SED fitting to improve the accuracy of SED fittings near our threshold. The AGN contributions can take any of the following values during the SED fitting, from 0.0 to 0.99 as shown in Table B1.

For the dust attenuation, we follow the same parameter set in Wang et al. (2020) instead of the one in Yang et al. (2023b). Yang et al. (2023b) reports that CIGALE may underestimate the redshift

compared with spec- z from CANDELS-EGS catalogue. However, to pursue an accurate estimation, we directly use spec- z from the CANDELS-EGS catalogue if available ($\sim 23\%$ of our sample). For the remaining no-spec- z sources, we give a range of redshift to allow CIGALE to estimate photo- z .

CIGALE provides a Bayesian estimation for the output of physical properties. This estimation considers all possible models to weigh a statistically-based physical property, while the best-fit SED output is based on the minimal χ^2 of the model. Statistically speaking, the Bayesian output is more reliable than the best fit. Yang et al. (2023b) also highlights the robustness of the Bayesian output. Therefore, in this paper, we choose the Bayesian output for the analysis rather than the best fit.

According to the Bayesian $f_{\text{AGN,IR}}$, we check the estimation quality. Fig. 2 displays the results. The median $f_{\text{AGN,IR}}$ and error for all sources are ~ 0.068 and ~ 0.075 , respectively. The error is not too large to affect our following analysis significantly as our selection criterion is $f_{\text{AGN,IR}} \geq 0.2$, making our selection less likely to be severely contaminated by SFG.

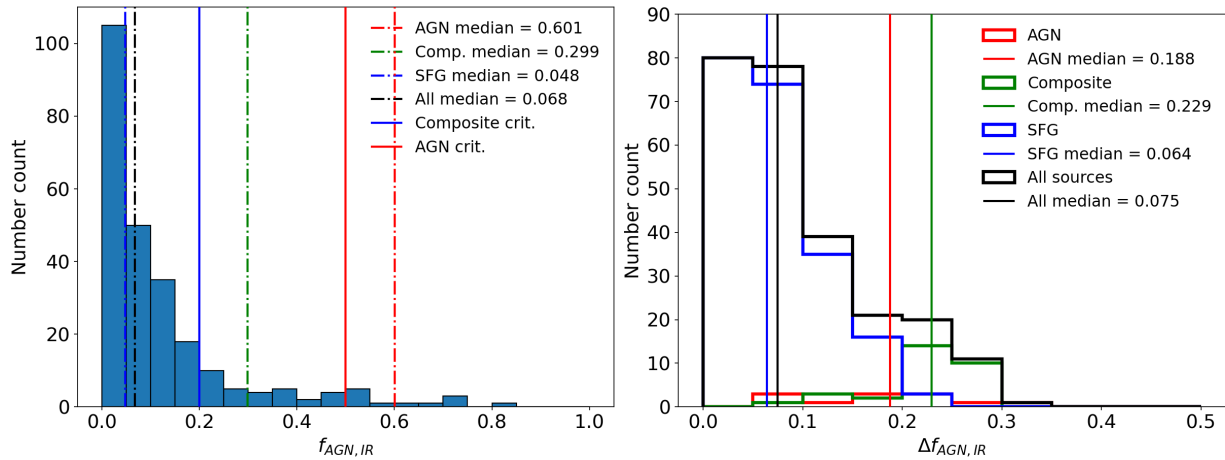


Figure 2. The histogram of $f_{\text{AGN,IR}}$ and its error. The left panel shows the distribution of $f_{\text{AGN,IR}}$. The solid lines mark the criteria for composite and AGN. The dot-dash lines show the median $f_{\text{AGN,IR}}$ of AGN, composite, SFG, and all sources, respectively. The right panel shows the error of $f_{\text{AGN,IR}}$ for AGN, composite, SFG, and all sources. The red, green, blue, and black solid lines are the median errors of $f_{\text{AGN,IR}}$ for AGN, composite, SFG, and all sources, respectively.

Fig. 1 displays the performance of SED fittings with their MIRI cutouts.

2.3 Sample selections

After our initial run of CIGALE on 573 sources we select our initial sample based on the SED fitting results.

First, our work mainly focuses on using mid-IR photometry to select AGNs, Yang et al. (2023b) provides a criterion that each source should be detected by at least 2 bands in *JWST* MIRI. However, to obtain a comprehensive AGN census and ensure that the MIR colour-colour diagram (e.g., Kirkpatrick et al. 2017) is available, we impose a more stringent constraint, requiring at least 3-band detection.

Additionally, since two of the pointings (observation ID: o012_t026 and o015_t028) miss $7\ \mu\text{m}$ and $21\ \mu\text{m}$ detection, we are unable to apply the $7\ \mu\text{m}$ 80% completeness flux limit, which has the faintest flux limit (Ling et al. 2022; Wu et al. 2023). Therefore, we adopt the second faintest $10\ \mu\text{m}$ 80% completeness flux limit (Ling et al. 2022; Wu et al. 2023) to exclude sources that fall below the flux limit. Some sources might have no $10\ \mu\text{m}$ detection by MIRI, so we substitute the estimated $10\ \mu\text{m}$ flux from CIGALE for undetected flux to make the completeness selection feasible and doable.

Finally, we check the performance of SED fittings and find out that there are 2 stars in the sample. In addition to stars, we find a source whose χ^2 is 9.6, which is larger than the median χ^2 of the rest of the sample (~ 1.14). After checking the image from the Hubble Space Telescope (*HST*), Spitzer, and *JWST*, this source shows no abnormality and is included in our final sample. In summary, we exclude 2 stars. 253 sources remain in the final sample. Fig. 3 shows the flowchart of our sample selections.

To define our sources as the candidates, we follow the same criterion as Wang et al. (2020), requiring $f_{\text{AGN,IR}} \geq 0.2$ for the candidates. We choose this criterion to enable a proper comparison with Wang et al. (2020) and to demonstrate the unprecedented sensitivity of *JWST* (e.g., Kim et al. 2021; Ho et al. 2021). Additionally, We divide our candidates into two based on the following criteria: composite ($0.2 < f_{\text{AGN,IR}} < 0.5$) and AGN ($f_{\text{AGN,IR}} \geq 0.5$). Among 42 candidates, 30 of them are composites and 12 of them are AGNs. The remaining 210 sources are classified as SFGs because of low AGN contributions ($f_{\text{AGN,IR}} < 0.2$).

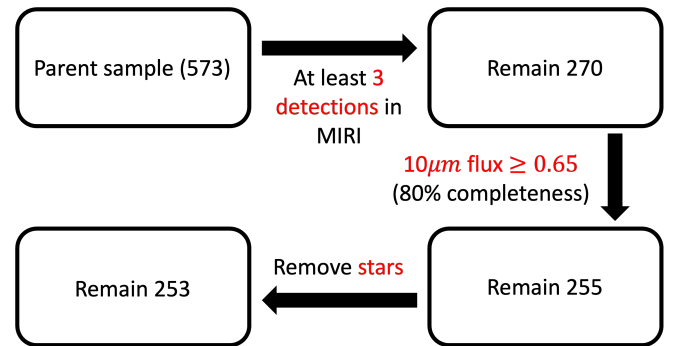


Figure 3. The flowchart of how we select our sample.

3 RESULTS AND DISCUSSION

3.1 The uncertainties of SED fittings

For the discussion on $f_{\text{AGN,IR}}$ in this work, the absence of FIR observations is a problem for SED fittings. The uncertainties may occur when the scientific results are analysed by physical properties estimated from SED fittings. To explore this influence, it is necessary to apply mock observations. In CIGALE, a mode called "savefluxes" can introduce a simulation to generate mock observations. We utilise the savefluxes model to generate 100 observations to analyse how significant the uncertainty is when the absence of FIR observations occurs. Table B2 lists the parameters applied to generate the mock observations. We set the majority of parameters to be one choice and merely change the AGN contribution and redshift since we focus on two crucial physical quantities in this work: AGN contribution and total IR luminosity to constrain the mock performance. Both quantities are strongly affected by the choice of AGN contribution and redshift parameters in CIGALE. Note that we set the redshift range from 0.5 to 1.0 rather than starting from 0.01 due to the avoidance of overflow in CIGALE if the redshift is smaller than 0.5.

We separate the mock observations into two groups. One group (hereafter, the group with-Herschel) contains the Spectral and Photometric Imaging Receiver (SPIRE, Griffin et al. 2010) PSW ($250\ \mu\text{m}$), PMW ($350\ \mu\text{m}$), and PLW ($500\ \mu\text{m}$) in the *Herschel* Space Observatory (*HSO*). The other group (hereafter, the group without-Herschel)

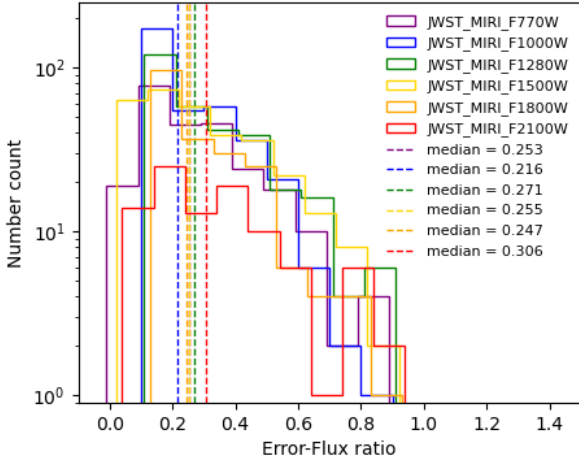


Figure 4. An example of the distributions of the error-flux ratio for JWST MIRI. The dashed lines show the median for each band.

does not. For the flux errors of the SPIRE mock observations, we adopt the $\text{SNR} = 40$ flux-error relation from Pokhrel et al. (2016) to calculate the errors. For the other bands, we calculate the error-flux ratio for each band in each source. Fig. 4 shows the distribution of the error-flux ratio for JWST as an example. We take the median value to generate the errors for each band.

Next, we utilise the parameter list in Table B1 to re-fit the SEDs for both groups and analyse their performance respectively. Fig. 5 shows their performance. Note that there are some small point displacements in both figures, this phenomenon is due to the choice of using Bayesian estimations for AGN contribution and total IR luminosity. Bayesian estimations can consider more situations than using input numbers. The estimated values for both groups are consistent according to the estimated values (for without-Herschel, $\sim 2.7\%$ smaller for AGN contribution and $\sim 7.5\%$ smaller for total IR luminosity) and the fitting slopes (1.031 for AGN contribution and 0.96 for total IR luminosity). However, for the error estimations, the median error of AGN contribution for the group with-Herschel (without-Herschel) is ~ 0.065 (~ 0.104); The median error of total IR luminosity is $\sim 9.7 \times 10^9$ ($\sim 1.47 \times 10^{10}$) in solar luminosity L_{\odot} . Fig. 6 shows detailed results, proving that the without-Herschel group estimates larger errors than the with-Herschel group ($\sim 65.2\%$ larger for AGN contribution and $\sim 52.1\%$ larger for total IR luminosity, both take the median value of the fraction in Fig. 6). It indicates that the catalogue in which FIR observations are absent surely enlarges the uncertainty of estimated physical properties. In conclusion, although the uncertainty of errors is enlarged, we claim that lacking FIR observations in this work does not largely and significantly change our conclusions. Additionally, compared with the with-Herschel group, the estimated total IR luminosity in the without-Herschel group seems to be slightly underestimated ($\sim 7.5\%$). The majority of points are below the ratio = 1.0. This underestimation might refer to the importance of FIR observations as well.

3.2 Source distribution

We start to discuss our fitting obtained through CIGALE. In the following subsections, we concentrate on two essential properties: AGN contribution and AGN number fraction. To establish the relations of

AGN contribution and AGN number fraction with other physical properties, we have depicted a preliminary picture of our sources distribution in Fig. 7. From Fig. 7, our AGN candidates are mostly located in higher redshift with higher AGN contribution rather than the composite candidates, which is consistent with the results in Toba et al. (2020). However, it is not sufficient to claim this relation. An advanced analysis is necessarily introduced. To determine whether there are relations between AGN contribution and total IR luminosity more specifically, we investigate both AGN contribution and AGN number fraction in §3.3 and §3.4, respectively, to obtain a clearer understanding of their relations.

In addition, we compare our candidates with those of Yang et al. (2023b), who, before our work, also utilised the same field and sample to select AGN candidates. However, their criteria were $0.1 \leq f_{\text{AGN,IR}} < 0.5$ for composite sources and $f_{\text{AGN,IR}} \geq 0.5$ for AGN. Applying these criteria to our candidates, the number of composites increases to 83, while the number of AGN remains at 12, yielding number ratios of $83/253 = 0.33 \pm 0.04$ and $12/253 = 0.047 \pm 0.014$, respectively. Yang et al. (2023b) identified 102 composite sources and 25 AGN from 560 sources, resulting in 0.18 ± 0.02 and 0.045 ± 0.009 ratios for composites and AGN, respectively. While the AGN ratios are consistent, our composite ratio is higher.

The exact reason for this difference is unclear, but possible sources include the fact that Yang et al. (2023b) used sources detected in at least two MIRI filters, whereas we required detections in three filters. This results in a smaller sample size for our analysis (253 vs. 560), which might lead to the selection of intrinsically brighter sources and a slightly larger fraction of composites. Furthermore, as shown in Fig. 2, the number of objects changes drastically with small variations in $f_{\text{AGN,IR}}$, which can occur due to slight differences in the fitting parameters between our analyses. This could also contribute to the observed difference in the fraction of composite sources.

3.3 AGN contribution

We calculate the average AGN contribution in each bin and check whether the relation between AGN contribution and redshift or total IR luminosity is clear or not. Note that we ignore the bins which have only one source for consistency and proper statistical meaning.

Fig. 8 illustrates AGN contribution as a function of redshift. The results in Wang et al. (2020) are depicted as well to show the comparison. It seems that the green and the orange group are increasing. However, if the p-value is considered, both exceed the p-value threshold ($p \leq 0.05$), which means that we cannot conclude a tight relation between AGN contribution and redshift in this work statistically. This discrepancy with Wang et al. (2020) might be due to the lack of sources. Therefore, a larger sample size is required, enabling us to study the relationship more exhaustively.

Fig. 9 is AGN contribution as a function of total IR luminosity. It seems that AGN contribution is decreasing with increasing luminosity, especially for the purple and blue groups. This result is inconsistent with Chiang et al. (2019). Chiang et al. (2019) reports that AGN contribution is increasing as the luminosity goes higher. Such difference might be due to the source distribution of the sample in this work. The majority of sources ($\sim 69.8\%$) are below $10^{11} L_{\odot}$, which are not the typical luminous infrared galaxies (LIRGs, Sanders & Mirabel 1996). We claim that this reason might be the key to link to the decreasing result. Besides, all groups extend their tails to their faint ends compared with Wang et al. (2020). This extension might be attributable to the level of sensitivity between AKARI and JWST. JWST has a high sensitivity that can capture many fainter galaxies than before, inferring the power of finding fainter AGNs in the Uni-

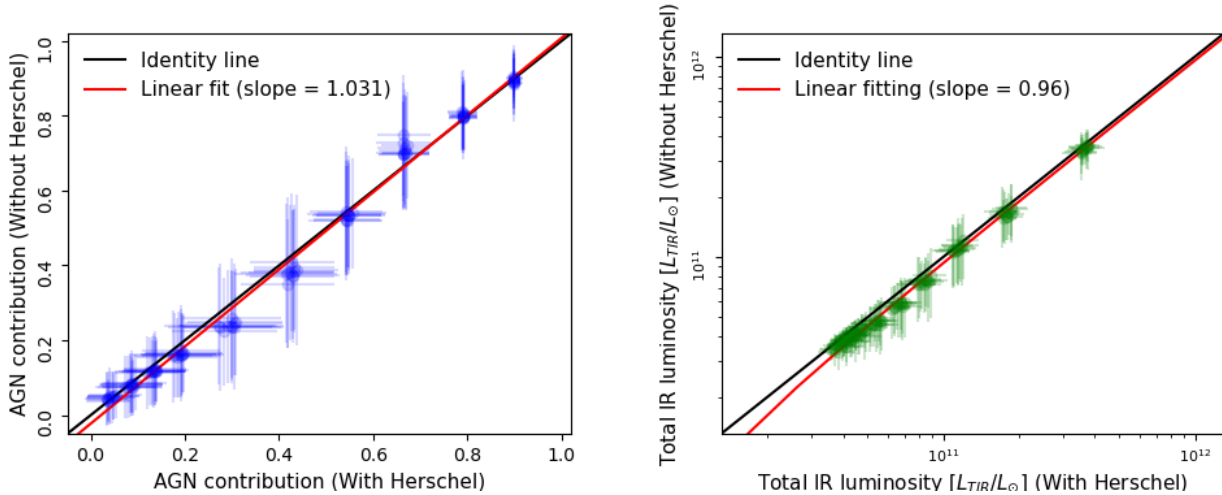


Figure 5. The comparison of both groups (with-Herschel and without-Herschel). The left panel shows the comparison of AGN contributions; The right panel shows the comparison of total IR luminosity. The solid black lines in the two panels represent the identity lines. The solid red line represents the linear fitting results.

verse. This achievement can allow us to investigate the evolution of AGNs and even the reionization of the Universe (Giallongo et al. 2015; Grazian et al. 2018) further. On the other hand, Fig. 9 might indicate that *JWST* has successfully accomplished our expectations.

3.4 AGN number fraction

AGN number fraction (f_{num}) can demonstrate how AGN populates in each redshift bin. The definition of AGN number fraction is presented in eq. 2:

$$f_{\text{num}} = \frac{N_{\text{Candidate}}}{N_{\text{Candidate}} + N_{\text{SFG}}}. \quad (2)$$

where $N_{\text{Candidate}}$ is the number of our composite candidates plus AGN candidates.

Fig. 10 shows our result. We compute the AGN number fraction in each bin and utilise the 1σ errors for small statistics presented in Gehrels (1986) to define the error bar for each bin. Wang et al. (2020) reports that AGN number fraction might have an increasing relation as a function of redshift. According to our results, only the orange group displays a low- p -value ($p \leq 0.05$) increasing relation. Nevertheless, the small sample size and small statistics make the uncertainty large enough to be unable to identify the truth of the trend. Kirkpatrick et al. (2023) reports that the AGN population is also increasing. However, their sample is also affected by the small statistics, making the uncertainty hard to constrain. In contrast, Hashiguchi et al. (2023) utilises much larger (~ 27000) sources to investigate the AGN number fraction in galaxy clusters. Their sample size is large enough to conclude a tightly increasing AGN number fraction against the redshift. To overcome the lack of sources, a larger mid-IR survey is necessary to increase more sources, lowering the difficulty of identifying scientific relations. However, the good news is that thanks to the high sensitivity of *JWST*, we can unearth more high- z galaxies that are difficult to observe by previous telescopes. Focusing on the blue, green, and orange groups, we conclude that we successfully extend and reveal the results in Wang et al. (2020) to the higher redshift. Besides, the result shows the difference between two different fields as well. 4 MIRI pointings ($\sim 8 \text{ arcmin}^2$) are much smaller than the NEP-wide field ($\sim 5.4 \text{ deg}^2$) in Wang et al. (2020),

the field of view limits the size of our sample in 4 MIRI pointings. This might be a key reason for our result.

In addition to redshift, we check AGN number fraction as a function of total IR luminosity shown in Fig. 11. Our result seems to have no obvious trends in different groups, which are consistent with Wang et al. (2020). Furthermore, none of the p -values for each group are smaller than 0.05, leading us to difficulty identifying the existence of trends between AGN number fraction and total IR luminosity. However, if we focus on the groups except for the orange group, these groups show higher AGN number fractions at each fainter end. Nevertheless, Kartaltepe et al. (2010) utilises *Spitzer* to investigate AGNs, reporting that the AGN number fraction is increasing at the ULIRGs and Hyper-luminous infrared galaxies (HyLIRGs ($L_{\text{TIR}} \geq 10^{13} L_{\odot}$), related work can be found in Gao et al. 2021). Chiang et al. (2019) concludes the same trend by *AKARI* as well, reporting the luminous sources are dominated by the AGN population. These discrepancies might be due to the sensitivity difference between the previous telescope and *JWST*, causing the previous works to be limited to low sensitivity. In this work, with the higher sensitivity of *JWST*, we can extend our understanding down to fainter galaxies ($L_{\text{TIR}} < 10^{11} L_{\odot}$), not just LIRGs or ULIRGs. Moreover, as we mentioned above, the majority of the luminosity of our sources ($\sim 69.8\%$) is not LIRGs. Consequently, combining the results in Fig. 9 and Fig. 11, they both suggest that we might successfully capture less luminous AGNs, which is a key goal (capturing fainter AGNs) in this work. This key result can lead us to believe that *JWST* can unearth more faint AGNs in the distant Universe (e.g., Harikane et al. 2023). The majority of sources in Wang et al. (2020) are LIRG and ULIRG due to the limitation of sensitivity for *AKARI*, and Kirkpatrick et al. (2023) reports the discovery of the population of mid-IR weak galaxies (where the mid-IR luminosity is mostly $\leq 10^{10} L_{\odot}$) in the high- z Universe. Combining with the results in this work, we can conclude that *JWST* truly reveals a new era of faint AGN research.

3.5 X-ray-selected AGNs

In this section, we briefly discuss the X-ray-selected AGNs in our sample. An X-ray survey called AEGIS-X Deep (AEGIS-XD) survey by *Chandra* X-ray observatory (Nandra et al. 2015) provides a

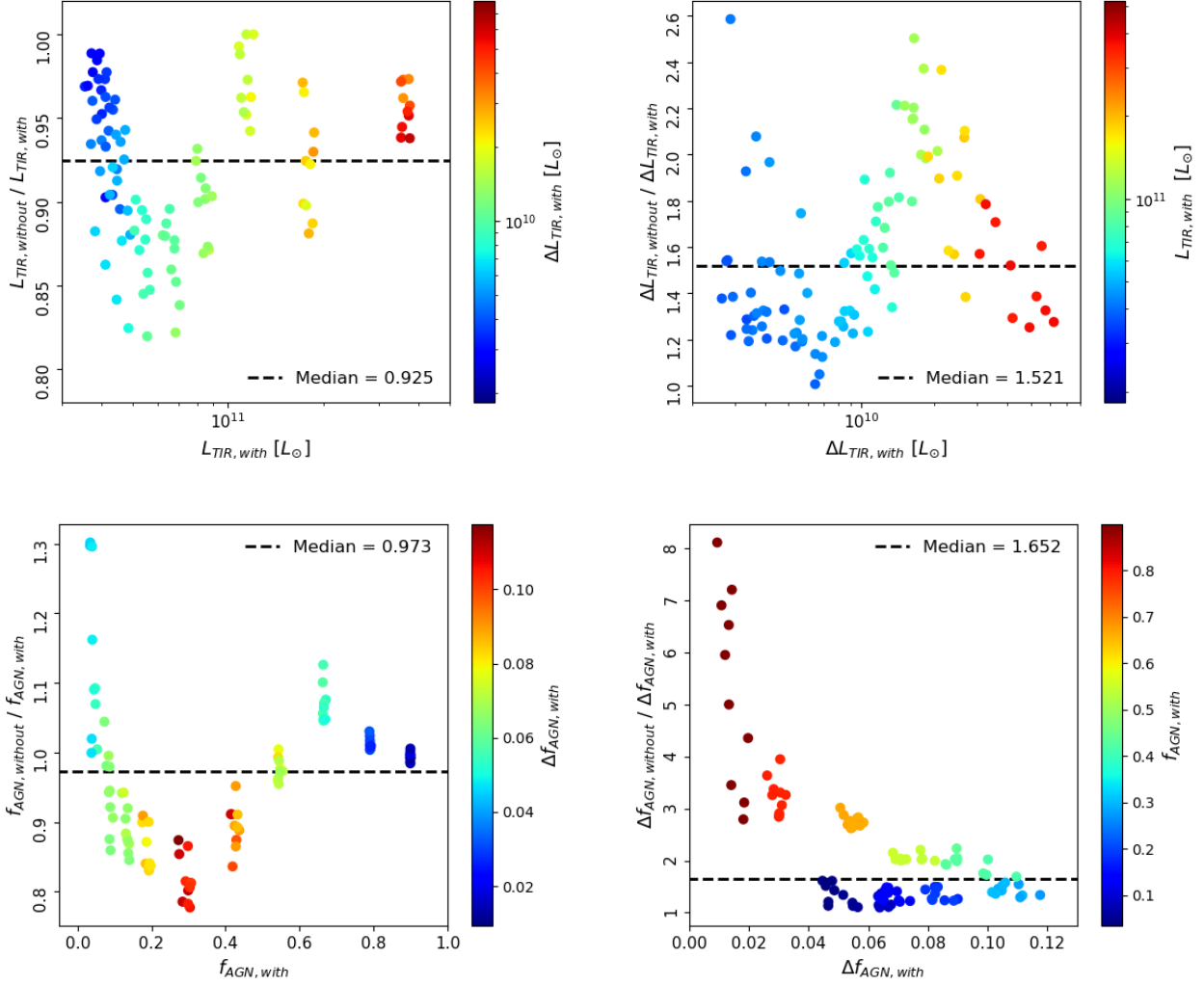


Figure 6. The detailed comparisons. The left panel compares total IR luminosity and AGN contribution; the right panel shows their error comparisons. The colour bar represents the corresponding errors or estimated values, respectively. The dashed black lines represent the median ratio for each block.

wild observation to investigate the properties of X-ray sources in the Universe, the CEERS field is within the survey area as well.

Among our sample, AEGIS-XD has 13 matched X-ray sources. Adopting the X-ray AGN criterion by X-ray luminosity $L_X \geq 10^{43}$ erg/s (Auge et al. 2023), we have 6 X-ray-selected AGN candidates and 4 of them are inside the candidates in this work ($\sim 66.6\%$). The remaining 2 sources are classified as SFGs by our selection criteria, moreover, their AGN contributions are minimal ($f_{\text{AGN,IR}} \leq 0.01$), which is quite lower than our criterion. Apart from the X-ray-selected AGNs, we still have 38 candidates not detected by the AEGIS-XD survey. However, with the MIRI on *JWST*, we complement the gap of using X-ray to select AGNs.

Besides, we investigate the relation between X-ray luminosity and total IR luminosity. Fig. 12 illustrates the relation, a slightly increasing trend is clear. To confirm whether the relation is statistically reasonable, we apply the p-value test for X-ray and total IR luminosity. The result shows $p = 0.928$, which is larger than 0.05, inferring that the relation in this work is statistically insignificant.

3.6 Colour-colour selections

Here we adopt the *JWST* MIRI colour-colour diagram for $z \sim 1$ ($0.75 \leq z < 1.25$), $z \sim 1.5$ ($1.25 \leq z < 1.75$), and $z \sim 2$ ($1.75 \leq z < 2.25$) from Kirkpatrick et al. (2017) and compare to its performance.

For the flux density ratio, we utilise the estimated flux value from CIGALE to replace the undetected flux for the feasible use of the colour-colour diagram. Kirkpatrick et al. (2017) provides different criteria to select these three objects: $f_{\text{AGN,MIR}} < 0.3$ as SFGs, $0.3 \leq f_{\text{AGN,MIR}} < 0.7$ as composites, and $f_{\text{AGN,MIR}} \geq 0.7$ as AGNs. Note that the aforementioned AGN contribution in §2.2 is defined in $8 - 1000\mu\text{m}$ for total IR luminosity. Kirkpatrick et al. (2017) uses AGN mid-IR contribution ($f_{\text{AGN,MIR}}$) which is defined in $5 - 15\mu\text{m}$ for mid IR luminosity. In Table B1, we do not particularly set the wavelength range of AGN contribution to be mid-IR range. Therefore, we integrate the mid-IR luminosity for dust emission and AGN emission from the best SED fitting result of our sample respectively, and calculate AGN mid-IR contribution using the same equation form as eq.1.

Fig. 13, Fig. 14, and Fig. 15 illustrate the results of our sample for both AGN mid-IR contribution and AGN contribution. The

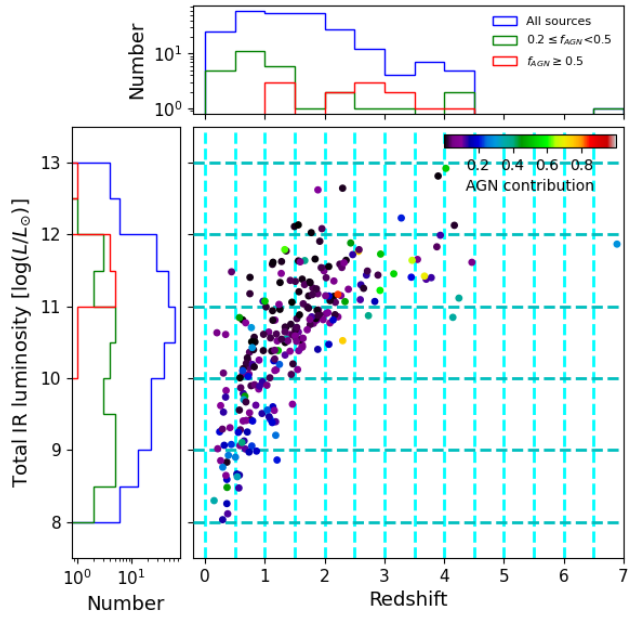


Figure 7. Total IR luminosity against redshift in this work. The histogram along the x-axis is the distribution of redshift. The histogram along the y-axis is the distribution of total IR luminosity in the logarithm. The colour bar shows the AGN contribution of each source. The cyan dashed lines cut the domain of redshift and total IR luminosity into several bins.

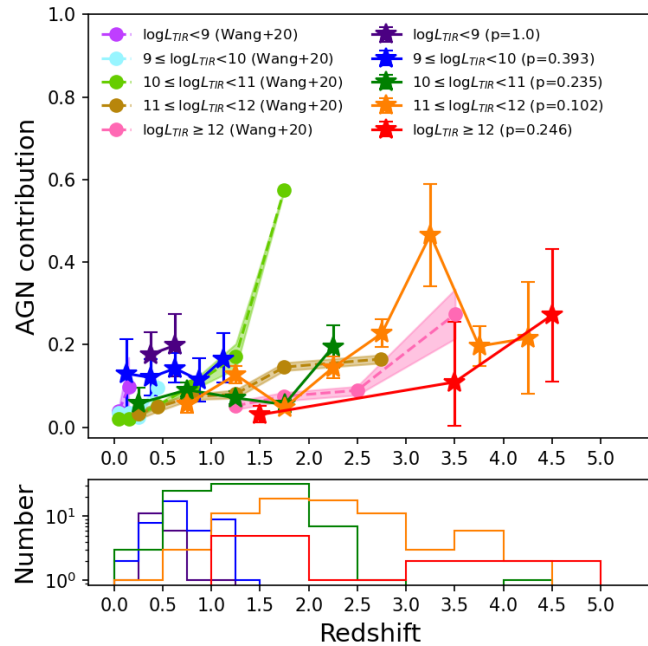


Figure 8. AGN contribution as a function of redshift. Circle markers are the results in Wang et al. (2020). Star markers are the results of this work. Purple is the $\log L_{\text{TIR}} < 9$ group. Blue is the $9 \leq \log L_{\text{TIR}} < 10$ group. Green is the $10 \leq \log L_{\text{TIR}} < 11$ group. Orange is the $11 \leq \log L_{\text{TIR}} < 12$ group. Red is the $\log L_{\text{TIR}} \geq 12$ group. The bottom panel shows the histogram for each bin in each group. Here we also show the p-value of each group.

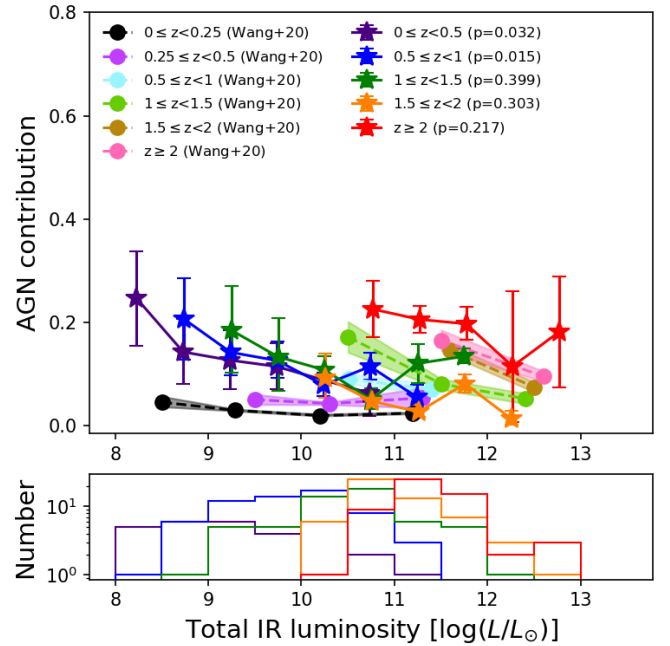


Figure 9. AGN contribution as a function of total IR luminosity. Circle markers are the results in Wang et al. (2020). Star markers are the results of this work. Purple is the $0 \leq z < 0.5$ group. Blue is the $0.5 \leq z < 1$ group. Green is the $1 \leq z < 1.5$ group. Orange is the $1.5 \leq z < 2$ group. Red is the $z \geq 2$ group. Black is the $0 \leq z < 0.25$ group in Wang et al. (2020) which is merged in the purple group in this work. The bottom panel shows the histogram for each bin in each group. Here we also show the p-value for each group.

majority of our candidates are successfully captured by the colour-colour diagram. However, Kirkpatrick et al. (2023) recently reported that this selection can be contaminated by SFGs and mid-IR weak galaxies which can pretend to be the AGN candidates or have unknown redshift. Therefore, Kirkpatrick et al. (2023) provides two new colour-colour selections (hereafter, MIR-only and NIR+MIR, respectively) to avoid these influences. We apply both methods to select the AGN candidates (hereafter, the cc-AGNs) and compare them with our candidates (hereafter, the SED-AGNs). Fig. 16 shows both results, having 32 (32) cc-AGNs for MIR-only (NIR+MIR) selection. The number of overlapped candidates with the SED-AGNs is 10 (15), showing some missed candidates in both the cc-AGNs and SED-AGNs. We check the missed candidates the SED-AGNs lose and the cc-AGNs lose. The SED-AGNs miss 22 (17) candidates and the cc-AGNs miss 32 (27) candidates.

Given the missed candidates, we check whether they are SFGs for each set of candidates. We focus on possibly the most problematic cases, six SED-AGNs that both cc-selections classified as SFGs. We crosscheck the SED results and the AGN contributions for the 6 candidates. These 6 SED-AGN candidates missed by the cc-selections exhibit small AGN contributions close to our selection criterion ($f_{\text{AGN,IR}} \sim 0.2$). Table 2 displays the detailed values and the relative errors. The errors are also large, while the best-fit AGN contributions for each source are also small at almost 0.0. As mentioned in §2.2, Bayesian $f_{\text{AGN,IR}}$ is considered more robust than the best-fit $f_{\text{AGN,IR}}$ statistically. With this consideration, the cc- and SED-AGNs are not overly inconsistent.

According to the above results, the cc-AGNs lose more candidates than the SED-AGNs, especially in the MIR selection. Kirkpatrick

Source ID	Bayesian $f_{\text{AGN,IR}}$	Best-fit $f_{\text{AGN,IR}}$
CANDELS_EGS_F160W_J141919.9+524851.5	0.25 ± 0.23	0.0
CANDELS_EGS_F160W_J141921.6+524839.1	0.21 ± 0.23	0.0
CANDELS_EGS_F160W_J142039.6+530330.7	0.21 ± 0.21	0.0
CANDELS_EGS_F160W_J141919.2+524858.7	0.24 ± 0.25	0.0
CANDELS_EGS_F160W_J141904.7+524853.8	0.22 ± 0.21	0.0
CANDELS_EGS_F160W_J141900.6+525002.9	0.22 ± 0.21	0.0

Table 2. The detailed information of the candidates that the cc-AGNs lose and are classified as the AGN candidates in this work.

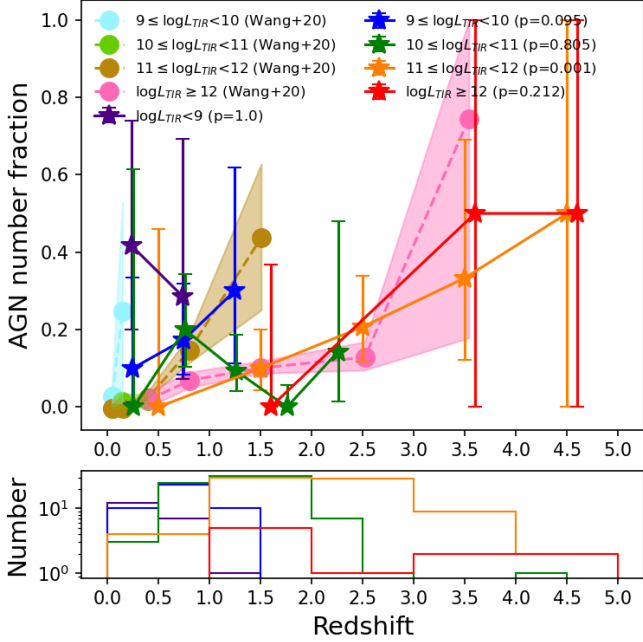


Figure 10. AGN number fraction as a function of redshift. Circle markers are the results in Wang et al. (2020). Star markers are the results of this work. Purple is the $\log L_{\text{TIR}} < 9$ group. Blue is the $9 \leq \log L_{\text{TIR}} < 10$ group. Green is the $10 \leq \log L_{\text{TIR}} < 11$ group. Orange is the $11 \leq \log L_{\text{TIR}} < 12$ group. Red is the $\log L_{\text{TIR}} \geq 12$ group. The bottom panel shows the histogram for each bin in each group. Here we also show the p-value of each group.

et al. (2023) mentions that the reliability of the NIR+MIR selection is higher than the MIR-only selection, which is consistent with our results. Additionally, Kirkpatrick et al. (2023) points out that applying the colour-colour selection in the small survey is not an efficient way to find AGNs, which agrees with our result of using MIR colour and NIR+MIR colour selection. Therefore, a larger survey (e.g., COSMOS-Web, Casey et al. 2023) is more suitable and might be a potentially useful data to apply colour-colour selections.

4 CONCLUSIONS

We utilised a multi-wavelength merged catalogue in the CEERS survey and performed CIGALE SED fittings to investigate the physical properties of our sample (253 sources after the selections). Applying our criteria, we found 42 candidates and separated them into two categories according to $f_{\text{AGN,IR}}$: 30 composites ($0.2 \leq f_{\text{AGN,IR}} < 0.5$) and 12 AGNs ($f_{\text{AGN,IR}} \geq 0.5$). We find previously reported relations in Wang et al. (2020) are not statistically obvious in this work due to their small sample size. This inconsistency might be attributed to the

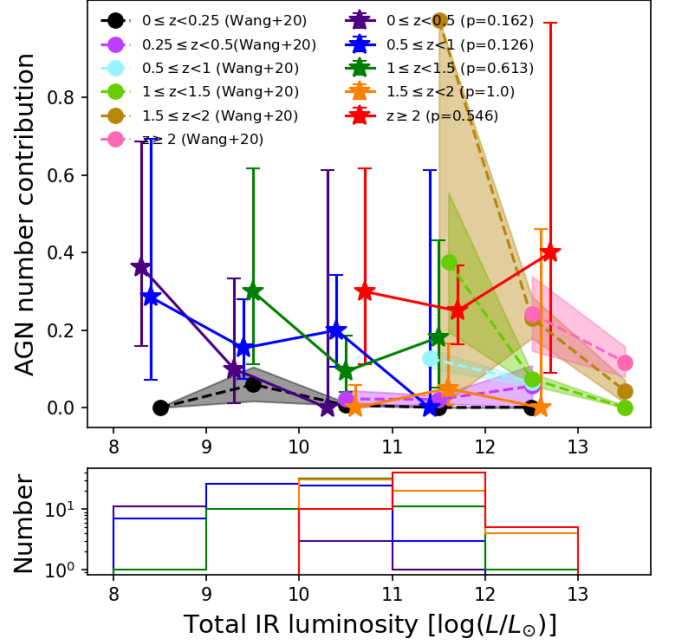


Figure 11. AGN number fraction as a function of total IR luminosity. Circle markers are the results in Wang et al. (2020). Star markers are the results of this work. Purple is the $0 \leq z < 0.5$ group. Blue is the $0.5 \leq z < 1$ group. Green is the $1 \leq z < 1.5$ group. Orange is the $1.5 \leq z < 2$ group. Red is the $z \geq 2$ group. Black is the $0 \leq z < 0.25$ group in Wang et al. (2020), which is merged in the purple group in this work. Note that the lowest- z bin for this work is $0 \leq z < 0.5$ due to small statistics. The bottom panel shows the histogram for each bin in each group. We also show the p-value for each group.

high sensitivity of JWST. JWST allows us to discover more fainter sources than previous works (Wang et al. 2020; Chiang et al. 2019; Kartaltepe et al. 2010).

In addition, we apply the MIRI colour-colour diagrams from Kirkpatrick et al. (2017) and Kirkpatrick et al. (2023), where the majority of our candidates located in $0.75 \leq z \leq 2.25$ are successfully captured by these diagrams. Recently, Kirkpatrick et al. (2023) introduced two more reliable colour-colour selections. They reported that the previous selection in Kirkpatrick et al. (2017) is unreliable and might be potentially affected by the contamination from SFGs and mid-IR weak galaxies. Moreover, it is also limited in certain redshift ranges, which is not general enough in the high- z Universe. Our findings reveal that the candidates with low AGN contribution ($f_{\text{AGN,IR}} < 0.5$, which is the composite candidates) failed to be identified as AGNs through colour-colour selections. This failure suggests that such methods might not be suitable for a small survey

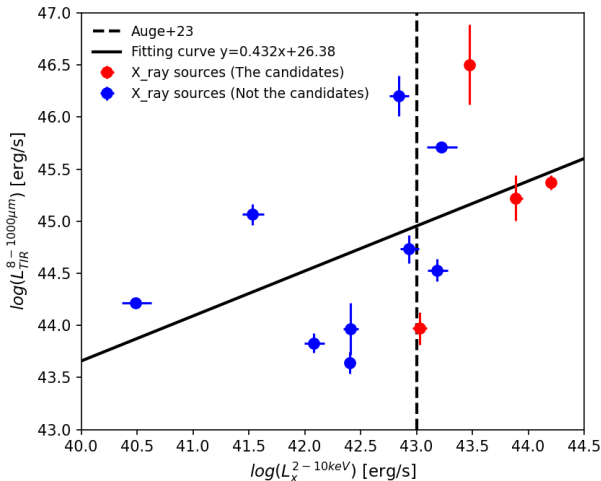


Figure 12. Relation between X-ray luminosity and total IR luminosity. The red dots are the candidates in this work. The blue dots are the SFGs in this work. The black dashed line shows the criterion of X-ray-selected AGN from [Auge et al. \(2023\)](#). The black solid line is the fitting curve.

like CEERS in this work, which is consistent with the conclusion from [Kirkpatrick et al. \(2023\)](#).

Note that the sample size in this work is not large enough (~ 573 sources), e.g., the relation in Fig. 11 is still not obvious. Therefore, a larger sample size is required to confirm the relations investigated in this work. With more *JWST* MIRI observations to be released, we expect that we can explore the properties of AGNs more accurately in the future.

ACKNOWLEDGEMENTS

The authors express their appreciation to the anonymous referee for the constructive comments and suggestions which significantly improved the quality of the paper.

TG acknowledges the support of the National Science and Technology Council of Taiwan through grants 108-2628-M-007-004-MY3, 110-2112-M-005-013-MY3, 112-2112-M-007-013, and 112-2123-M-001-004-. TH acknowledges the support of the National Science and Technology Council of Taiwan through grants 110-2112-M-005-013-MY3, 110-2112-M-007-034-, 111-2123-M-001-008-, 110-2112-M-005-013-MY3, 110-2112-M-007-034-, and 112-2123-M-001-004-. SH acknowledges the support of The Australian Research Council Centre of Excellence for Gravitational Wave Discovery (OzGrav) and the Australian Research Council Centre of Excellence for All Sky Astrophysics in 3 Dimensions (ASTRO 3D), through project number CE17010000 and CE170100013, respectively.

This work is based on observations made with the NASA/ESA/CSA James Webb Space Telescope. The data were obtained from the Mikulski Archive for Space Telescopes at the Space Telescope Science Institute, which is operated by the Association of Universities for Research in Astronomy, Inc., under NASA contract NAS 5-03127 for *JWST*. These observations are associated with program *JWST*-ERS01345. This work is based on observations taken by the CANDELS Multi-Cycle Treasury Program with the NASA/ESA HST, which is operated by the Association of Universities for Research in Astronomy, Inc., under NASA contract NAS 5-26555.

This work used high-performance computing facilities operated by the Centre for Informatics and Computation in Astronomy (CICA) at National Tsing Hua University. This equipment was funded by the Ministry of Education of Taiwan, the National Science and Technology Council of Taiwan, and the National Tsing Hua University.

DATA AVAILABILITY

The MIRI observations from *JWST* CEERS survey are publicly available at the MAST archive <https://mast.stsci.edu/portal/Mashup/Clients/Mast/Portal.html>. The EGS Multi-Band Source and Photometric Redshift catalogue can be downloaded at <https://archive.stsci.edu/hlsp/candels/egs-catalogs>. Other data utilised in this work can be provided by request to the authors.

REFERENCES

- Arnouts S., Cristiani S., Moscardini L., Matarrese S., Lucchin F., Fontana A., Giallongo E., 1999, *MNRAS*, **310**, 540
- Ashby M. L. N., et al., 2015, *ApJS*, **218**, 33
- Auge C., et al., 2023, *arXiv e-prints*, p. [arXiv:2308.10710](https://arxiv.org/abs/2308.10710)
- Bielby R., et al., 2012, *A&A*, **545**, A23
- Blandford R., Meier D., Readhead A., 2019, *Annual Review of Astronomy and Astrophysics*, **57**, 467
- Boquien M., Burgarella D., Roehlly Y., Buat V., Ciesla L., Corre D., Inoue A. K., Salas H., 2019, *A&A*, **622**, A103
- Casey C. M., et al., 2023, *ApJ*, **954**, 31
- Chang Y.-Y., et al., 2017, *ApJS*, **233**, 19
- Chiang C.-Y., Goto T., Hashimoto T., Kim S. J., Matsuhara H., Oi N., 2019, *PASJ*, **71**, 31
- Comastri A., 2004, in Barger A. J., ed., *Astrophysics and Space Science Library* Vol. 308, Supermassive Black Holes in the Distant Universe. p. 245 ([arXiv:astro-ph/0403693](https://arxiv.org/abs/astro-ph/0403693)), doi:[10.1007/978-1-4020-2471-9_8](https://doi.org/10.1007/978-1-4020-2471-9_8)
- Cowley W. I., Baugh C. M., Cole S., Frenk C. S., Lacey C. G., 2018, *MNRAS*, **474**, 2352
- Fazio G. G., et al., 2004, *ApJS*, **154**, 10
- Feltre A., et al., 2013, *MNRAS*, **434**, 2426
- Finkelstein S. L., et al., 2017, The Cosmic Evolution Early Release Science (CEERS) Survey, *JWST* Proposal ID 1345. Cycle 0 Early Release Science
- Gao F., et al., 2021, *A&A*, **654**, A117
- Gehrels N., 1986, *ApJ*, **303**, 336
- Giallongo E., et al., 2015, *A&A*, **578**, A83
- Grazian A., et al., 2018, *A&A*, **613**, A44
- Griffin M. J., et al., 2010, *A&A*, **518**, L3
- Grogin N. A., et al., 2011, *ApJS*, **197**, 35
- Gruppioni C., Pozzi F., Zamorani G., Vignali C., 2011, *MNRAS*, **416**, 70
- Gu Y., Fang G., Yuan Q., Cai Z., Wang T., 2018, *ApJ*, **855**, 10
- Gwyn S. D. J., 2012, *AJ*, **143**, 38
- Harikane Y., et al., 2023, A *JWST*/NIRSpec First Census of Broad-Line AGNs at $z=4-7$: Detection of 10 Faint AGNs with $M_{BH} \sim 10^6 - 10^8 M_{\odot}$ and Their Host Galaxy Properties ([arXiv:2303.11946](https://arxiv.org/abs/2303.11946))
- Hashiguchi A., et al., 2023, *PASJ*, **75**, 1246
- Ho S. C. C., et al., 2021, *MNRAS*, **502**, 140
- Ilbert O., et al., 2006, *A&A*, **457**, 841
- Kartaltepe J. S., et al., 2010, *ApJ*, **709**, 572
- Kennicutt Robert C. J., 1998, *ARA&A*, **36**, 189
- Kim S. J., et al., 2019, *PASJ*, **71**, 11
- Kim S. J., et al., 2021, *MNRAS*, **500**, 4078
- Kirkpatrick A., et al., 2017, *ApJ*, **849**, 111
- Kirkpatrick A., et al., 2023, *ApJ*, **959**, L7
- Koekemoer A. M., et al., 2011, *ApJS*, **197**, 36
- Ling C.-T., et al., 2022, *MNRAS*, **517**, 853

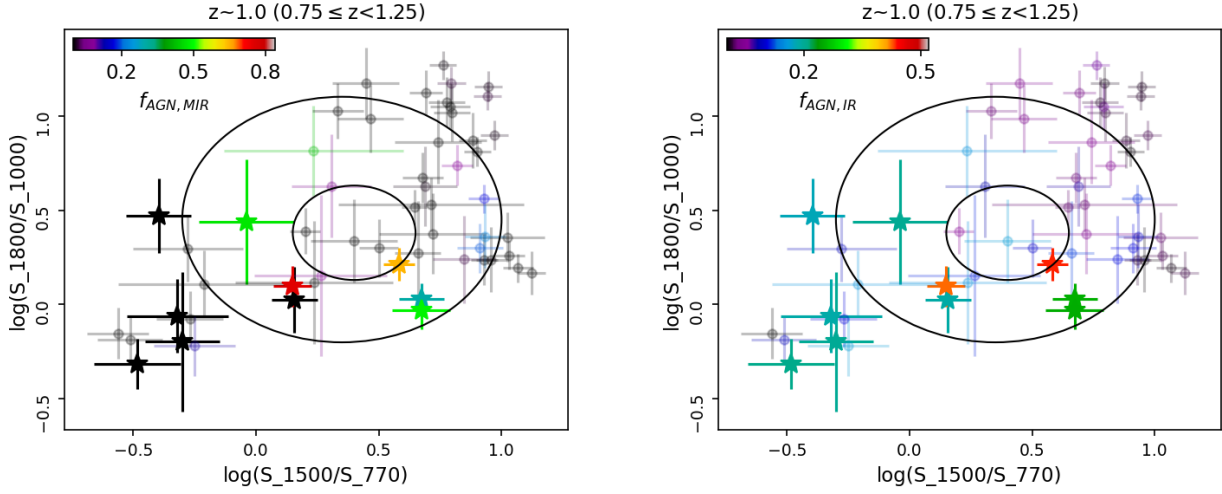


Figure 13. Colour-colour diagram at $z \sim 1$ ($0.75 \leq z < 1.25$). The left panel shows the AGN mid-IR contribution ($f_{\text{AGN,MIR}}$) for each source. The right panel shows the AGN contribution ($f_{\text{AGN,IR}}$) for each source as well. Three regions divided by outer and inner circles present the SFGs, composites, and AGNs criterion from outside to inside defined in Kirkpatrick et al. (2017), respectively. The star markers are the candidates in this work.

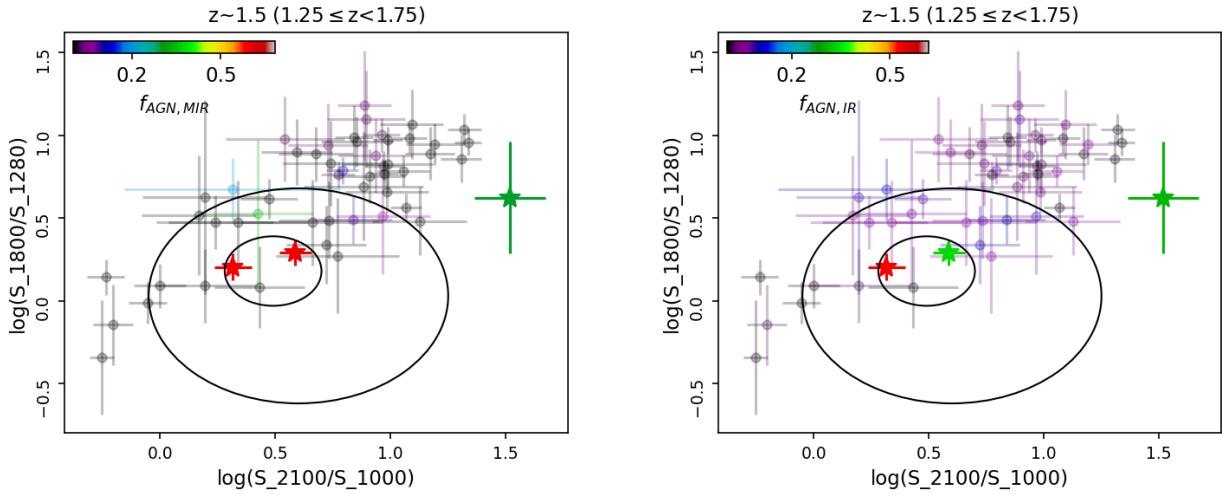


Figure 14. Colour-colour diagram at $z \sim 1.5$ ($1.25 \leq z < 1.75$).

Ling C.-T., et al., 2024, Exploring the faintest end of mid-infrared luminosity functions up to $z \approx 5$ with the JWST CEERS survey ([arXiv:2402.05386](https://arxiv.org/abs/2402.05386))
 Lyu J., et al., 2024, *ApJ*, 966, 229
 Matsuhara H., et al., 2006, *PASJ*, 58, 673
 Murakami H., et al., 2007, *PASJ*, 59, S369
 Nandra K., et al., 2015, *ApJS*, 220, 10
 Netzer H., 2015, *ARA&A*, 53, 365
 Planck Collaboration et al., 2020, *A&A*, 641, A6
 Pokhrel R., et al., 2016, *MNRAS*, 461, 22
 Rieke G. H., et al., 2015, *PASP*, 127, 665
 Rieke G., Alberts S., Lyu J., Morrison J., Shivaee I., 2017, MIRI in the Hubble Ultra-Deep Field, JWST Proposal. Cycle 1, ID. #1207
 Rigby J., et al., 2023, *PASP*, 135, 048001
 Salpeter E. E., 1955, *ApJ*, 121, 161
 Sanders D. B., Mirabel I. F., 1996, *ARA&A*, 34, 749
 Skelton R. E., et al., 2014, *ApJS*, 214, 24
 Stefanon M., et al., 2017, *ApJS*, 229, 32
 Toba Y., et al., 2020, *ApJ*, 899, 35

Treister E., Urry C. M., Schawinski K., Cardamone C. N., Sanders D. B., 2010, *ApJ*, 722, L238
 Wang T.-W., et al., 2020, *MNRAS*, 499, 4068
 Wu C. K. W., et al., 2023, *MNRAS*, 523, 5187
 Yang G., et al., 2023a, CEERS MIRI Imaging: Data Reduction and Quality Assessment ([arXiv:2307.14509](https://arxiv.org/abs/2307.14509))
 Yang G., et al., 2023b, *ApJ*, 950, L5

APPENDIX A: THE CUTOUTS OF AGN CANDIDATES

Here we show the cutouts of the AGN candidates ($f_{\text{AGN,IR}} \geq 0.5$) by each pointings in Fig. A1, Fig. A2, Fig. A3, and Fig. A4.

APPENDIX B: CIGALE PARAMETER LIST

In this appendix section, we list out the parameters used in SED fitting and generating mock observations in Table B1 and Table B2.

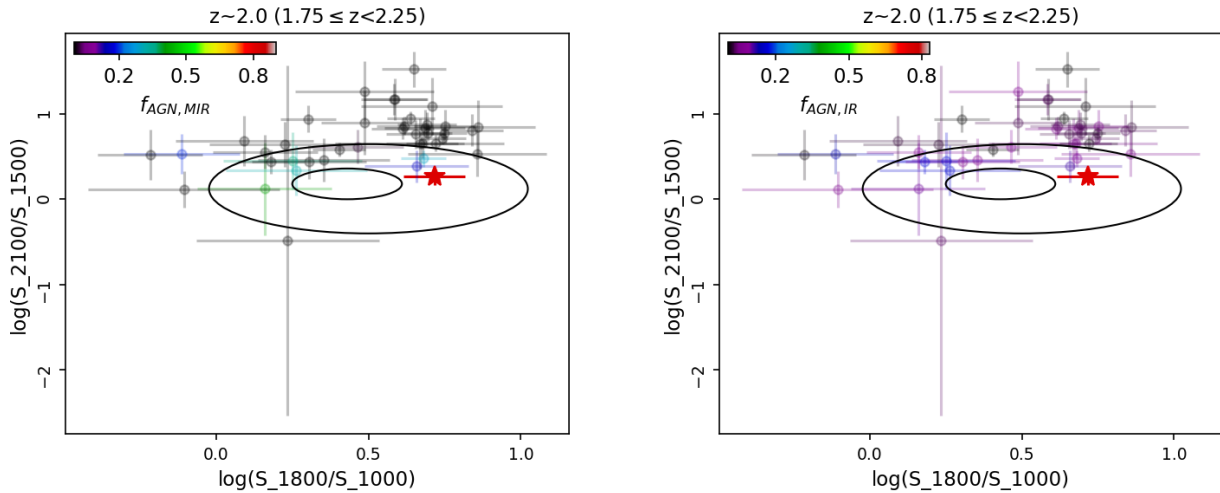


Figure 15. Colour-colour diagram at $z \sim 2$ ($1.75 \leq z < 2.25$).

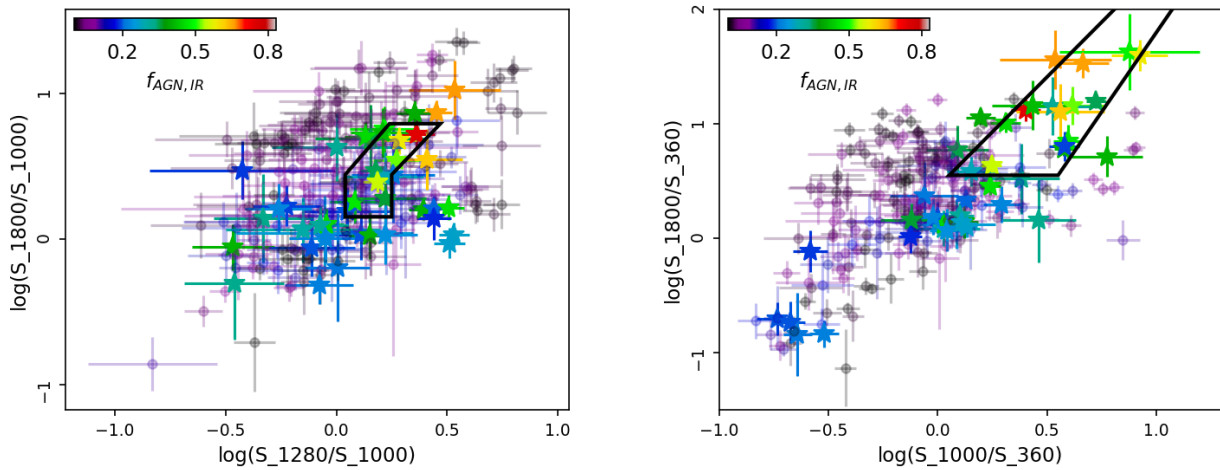


Figure 16. Two new colour-colour selections from Kirkpatrick et al. (2023). The left panel shows the new mid-IR selection which is not limited by the redshift; The right panel shows the near-IR + mid-IR combination. The near-IR band is IRAC1 in *Spitzer* (Fazio et al. 2004). The star markers are the candidates in this work. The black polygons display both AGN criteria defined in Kirkpatrick et al. (2023), respectively.

This paper has been typeset from a $\text{\TeX}/\text{\LaTeX}$ file prepared by the author.

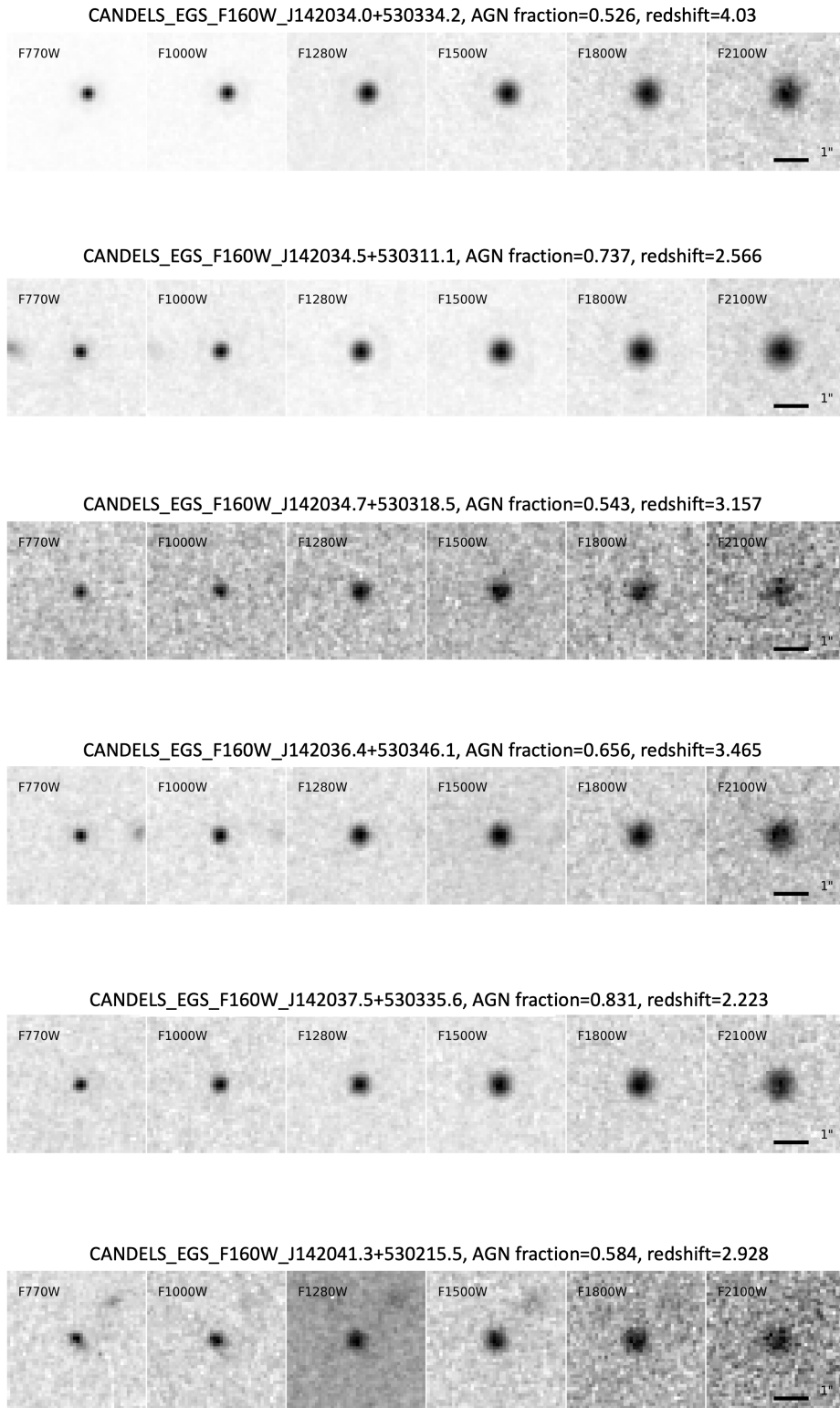


Figure A1. The AGN cutouts in the CEERS field pointings 1 (observation ID: o001_t021).

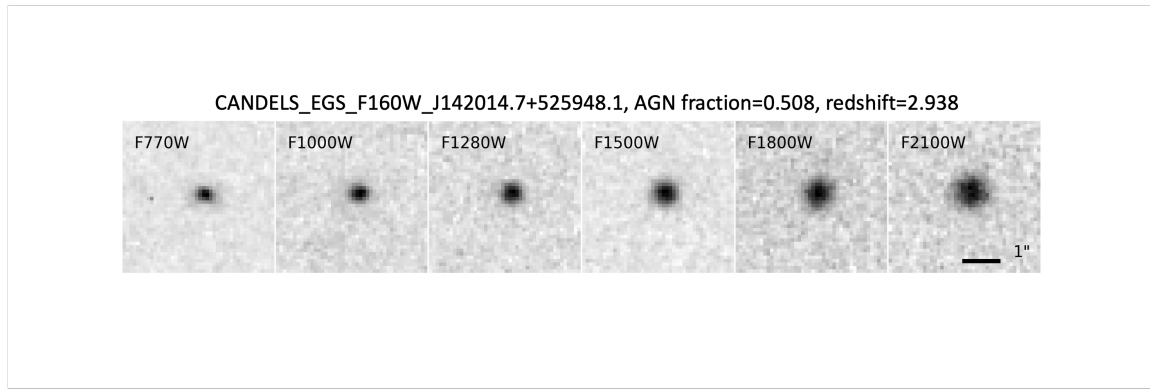


Figure A2. The AGN cutout in the CEERS field pointings 2 (observation ID: o002_t022).

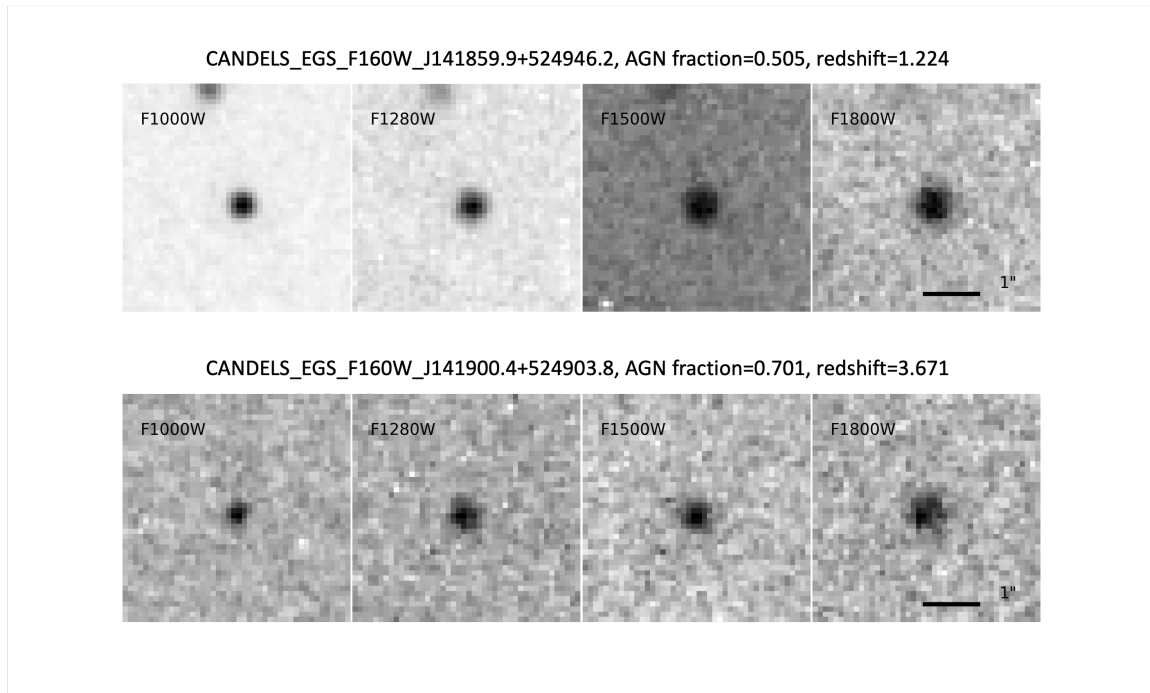


Figure A3. The AGN cutouts in the CEERS field pointings 5 (observation ID: o012_t026).

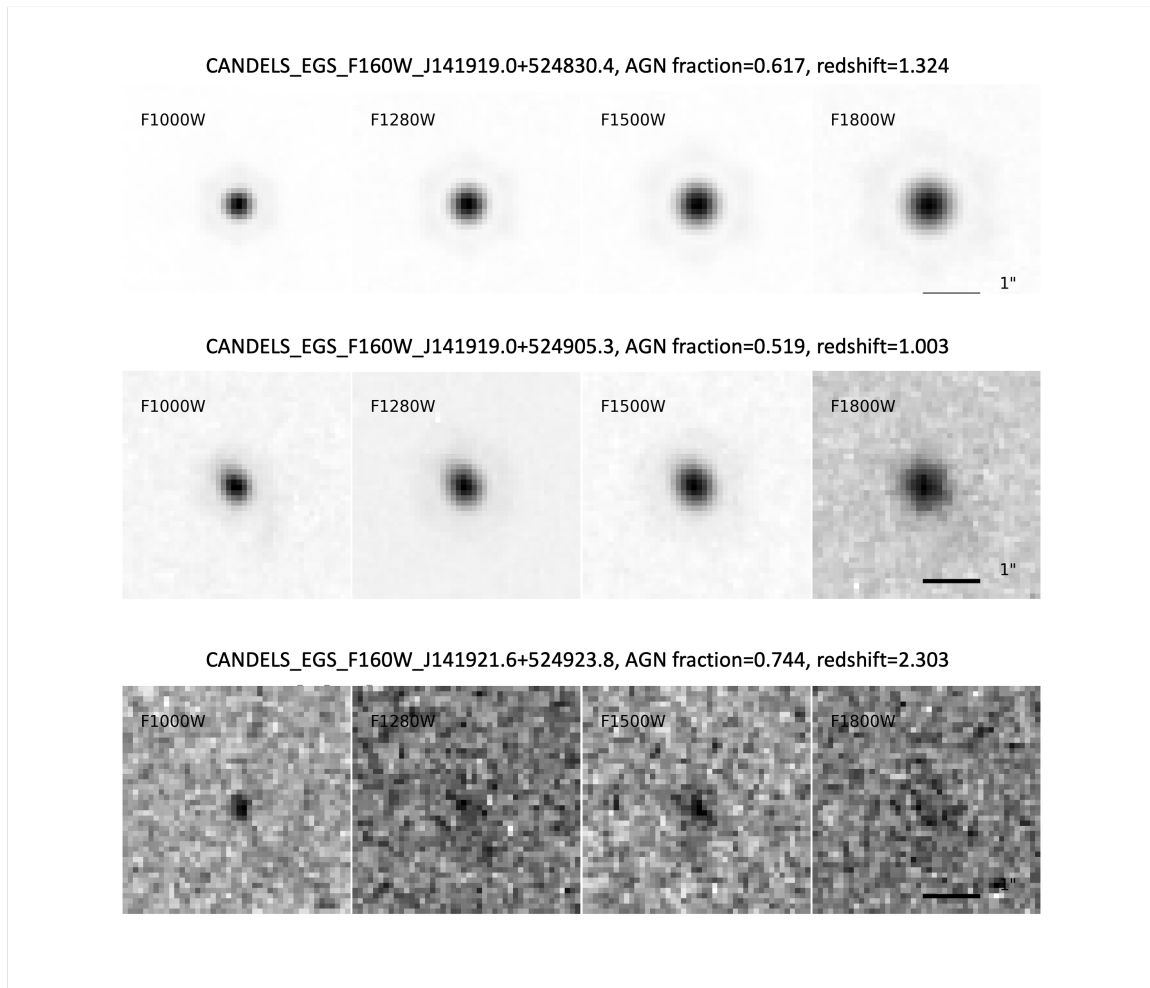


Figure A4. The AGN cutouts in the CEERS field pointings 8 (observation ID: o015_t028).

Module	Parameter	Values
sfhdelayed	τ_{main} (Myr)	100.0, 1000.0, 2000.0, 3000.0, 4000.0, 5000.0
...	age _{main} (Myr)	100.0, 200.0, 500.0, 1000.0, 2000.0, 3000.0, 4000.0, 5000.0
...	τ_{burst} (Myr)	50.0
...	age _{burst} (Myr)	20.0
...	f _{burst}	0.0
...	sfr _A	1.0
bc03	Initial mass function	Salpeter (1955)
...	metallicity	0.02
...	separation_age	10
dustatt_modified_CF00	$A_{\text{v_ISM}}$ (log scale)	-2.0 to 1.0 (10 steps)
...	μ	0.44
...	slope_ISM	-0.5, -0.7, -0.9
...	slope_BC	-0.7, -1.0, -1.3
nebular	logU	-2.0
...	Gas metallicity	0.02
dl2014	q _{PAH}	0.47, 2.50, 7.32
...	U _{min}	0.1, 1.0, 10.0, 50.0
...	α	2.0
...	γ	0.01, 0.02, 0.05, 0.1, 0.2, 0.5, 0.9
skirtor2016	Optical depth at 9.7 μm (τ)	3, 5, 7, 9, 11
...	Opening angle	40
...	Inclination	70
...	$f_{\text{AGN,IR}}$	0.0, 0.01, 0.05, 0.1, 0.13, 0.15, 0.18, 0.2
...		0.3, 0.4, 0.5, 0.6, 0.7, 0.8, 0.9, 0.99
redshift	redshift	0.01-7.0 (100 steps) for no-spec-z sources

Table B1. Model parameters, note that parameters which are not listed here remain default.

Module	Parameter	Values
sfhdelayed	τ_{main} (Myr)	500.0
...	age _{main} (Myr)	4000.0
dustatt_modified_CF00	$A_{\text{v_ISM}}$ (log scale)	1.0
...	slope_ISM	-0.5
...	slope_BC	-1.3
dl2014	q _{PAH}	7.32
...	U _{min}	0.1
...	α	2.0
...	γ	0.01
skirtor2016	Optical depth at 9.7 μm (τ)	11
...	$f_{\text{AGN,IR}}$	0.0-0.9 (10 steps)
redshift	redshift	0.5-1.0 (10 steps)

Table B2. Model parameters used to generate mock observations. Parameters that are not listed here remain default and identical to Table B1.